Spin-Dependent Charge-Carrier Recombination Processes in Tris(8-Hydroxyquinolinato) Aluminum

H. Popli, X. Liu, T.H. Tennahewa, M.Y. Teferi, E. Lafalce, H. Malissa,* Z.V. Vardeny, and C. Boehme

Department of Physics and Astronomy, University of Utah, Salt Lake City, Utah 84112, USA

(Received 2 April 2020; revised 25 June 2020; accepted 20 July 2020; published 3 September 2020)

We study the nature and dynamics of spin-dependent charge-carrier recombination in tris(8-hydroxyquinolinato) aluminum (Alq_3) films in light-emitting diodes at room temperature using continuous-wave and pulsed electrically detected magnetic resonance (EDMR) spectroscopy. We find that the EDMR signal is dominated by an electron-hole recombination process and another weaker EDMR signal, the fundamental nature of which is investigated. From the pulsed EDMR measurements, we obtain a carrier-spin-relaxation time, $T_2 = 45\ \text{ns} \pm 25\ \text{ns}$, which is much shorter than that of T_2 in conjugated polymers, but relatively long for a molecule containing elements with a high atomic number. Using multifrequency continuous-wave EDMR spectroscopy, we obtain the local hyperfine field distributions for electrons and holes, as well as their respective spin-orbit-coupling-induced g-factor and g-strain values.

DOI: 10.1103/PhysRevApplied.14.034012

I. INTRODUCTION

The interest in organic semiconductor (OSEC)-based spintronics devices [1–3] has led to extensive studies of these materials' optoelectronic [4] and magnetoelectronic properties [5,6]. Electronic excitations in OSECs generally exhibit weak spin-orbit coupling (SOC), and, consequently, charge-carrier transport, recombination, and spin-transport mechanisms can be dominated by spin-selection rules. There are ample examples of such spin-dependent processes [7–14] in OSECs, which involve localized spin-1/2 carriers or polarons (P^+ and P^-) [7], weakly coupled polaron pairs (P^+P^-) [11,15], as well as more complex paramagnetic electronic excitations, such as trions and spin triplet-polaron complexes [16]. One important experimental technique for the study of such spin-dependent processes in OSECs have been electron paramagnetic resonance–based techniques, including optically (ODMR) and electrically (EDMR) detected magnetic resonance spectroscopies [9,16–18]. Detailed knowledge of the relevant spin-dependent recombination processes in these material systems is required for technological applications, e.g., magnetic-resonance-based magnetometry at low magnetic fields and room temperature, which provides pathways for calibration-free robust, which means material-degradation independent, absolutely offset-free magnetic field sensors [19].

Here, we present a study of spin-dependent electronic transitions in thin solid films based on tris-(8-hydroxyquinolinato) aluminum (Alq_3), a small molecule that consists of a central aluminum atom with three side groups ($C_{27}H_{18}AlN_3O_3$). Alq_3 is used as an electroluminescent layer in high-efficiency organic light-emitting diodes (OLEDs) [20] and other applications, such as spin valves [21] and light-emitting transistors [22]. In the past, the nature of charge carriers and spin-dependent charge-carrier recombination in Alq_3-based OLEDs has already been studied with continuous-wave (cw) EDMR and ODMR spectroscopies [23–25], revealing that charge carriers in Alq_3 films form polarons, and the precursor excitations to exciton generation are polaron pairs [25]. It has also been claimed that other excitations, such as bipolarons (BP^+ and BP^-) and triplet excitons, may contribute to spin-dependent recombination [26,27].

Following our previous studies on spin-dependent electronic processes in OLEDs based on π-conjugated polymers using transient EDMR techniques [8,28,29], the study presented here is motivated by the idea to gain new insights into the nature of spin-dependent transitions in Alq_3 by application of a broad regime of magnetic resonance techniques, including multifrequency and pulsed coherent spin-manipulation experiments to the study of Alq_3. As Alq_3 is a small molecule and not a conjugated polymer, and it has a high density of Al, an element with a high atomic number. Thus, we hypothesize that electronic spin states in Alq_3 exhibit a much higher SOC, when compared with that of π-conjugated polymers, and that this affects the physical behavior of spin-dependent processes. Using pulsed and multifrequency EDMR spectroscopies [30], including electrically detected Hahn-echo experiments, electrically detected spin-Rabi oscillation measurements and other coherent spin-motion experiments

*hans.malissa@utah.edu

[11,31], we study charge-carrier spin-relaxation times and compare them to other OSECs with high atomic numbers, e.g., Pt-rich polymers [32].

II. EXPERIMENTS

OLEDs with active layers of Alq_3 are prepared on glass templates with lithographically defined thin-film wiring based on indium tin oxide (ITO), as described by McCamey *et al.* [30]. For their preparation, 50-nm-thick layers of poly(3,4-ethylenedioxythiophene):poly(styrenesulfonate) (PEDOT:PSS), which serve as hole injectors, are deposited on ITO contact pads by spin casting and subsequent annealing at 110°C for 15 min. Alq_3 layers with thicknesses of about 30 nm are then deposited by thermal evaporation for about 3 min at a base pressure of about 10^{-7} mbar, using a tungsten basket and quartz cuvette in the evaporator. Finally, 7-nm-thick calcium electron-injection layers and 100 nm aluminium top electrodes are thermally evaporated, before these devices are encapsulated with SiO_2 insulating layers. The finished devices emitted green electroluminescence under application of sufficient bias voltages. To ensure bipolar charge-carrier injection, all devices are characterized by measurements of their I-V characteristics using a Keithley 2400 source meter. Figure 1(a) shows the Alq_3 OLED layer structure, a picture and a schematic of an OLED device under operation, the measured luminescence spectrum of one of the used Alq_3 devices, as well as the representative I-V curve.

We first carry out pulsed EDMR experiments, in which the OLED device current under constant voltage bias is recorded as a function of time after a brief (ns range) high-power microwave (MW) pulse (X band, ∼9.7 GHz), and magnetic field. For magnetic fields that are not in resonance with the MW excitation, the device current remains nearly constant after the brief pulse excitation. Under magnetic resonance conditions, transitions between spin states are induced by the MW fields, causing a change, ΔI, to the spin-dependent device current I, which reflects the transient behavior of charge-carrier recombination and, thus, the spin dynamics, as well as some of the electrical characteristics of the device, while the magnetic field dependence of these current changes reflect the spectral line shape of the resonance [26,33].

Pulsed EDMR experiments are carried out using a commercial Bruker ElexSys E580 spectrometer. For the pulsed operation, short high-power MW pulses are applied to the device under operation in the FlexLine ER 4118X-MD-5W1 dielectric resonator inside an Oxford CF935 cryostat to allow for measurements between 5 K and room temperature. The device bias voltage is provided by a Stanford Research Systems SIM928 isolated battery source, which is adjusted to voltages ranging from 3 to 20 V, while the OLED current is measured by an SR570 transimpedance amplifier with a gain of 2 μA/V. The experimental setup is

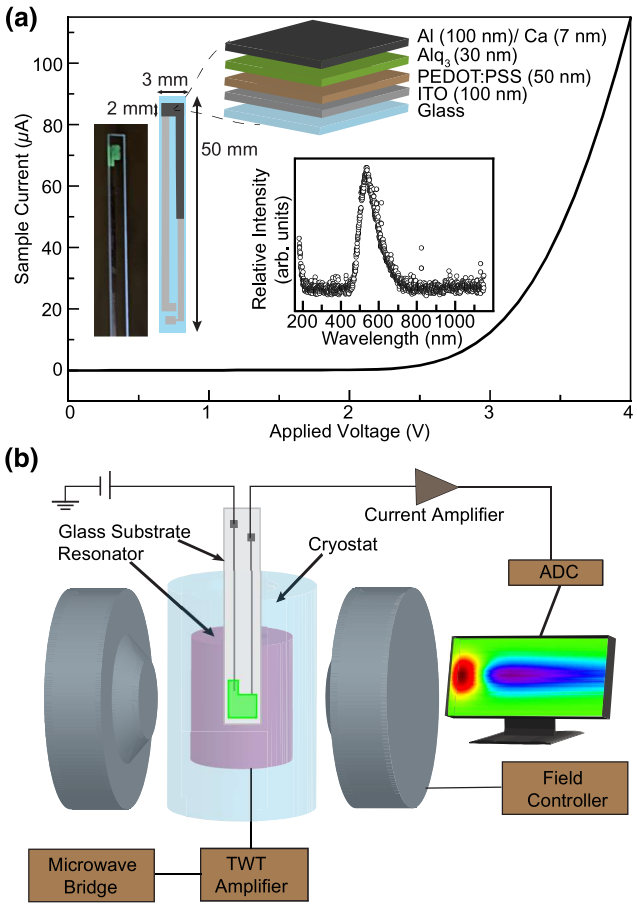

FIG. 1. Alq_3 device characterization and experimental setup. (a) Representative I-V curve of one of the studied devices. Insets show a photograph of a device under operation, its luminescence spectrum, and its layer structure, as well as a schematic including dimensions of the OLED device on a narrow glass substrate. This structure consists of PEDOT:PSS on ITO as hole-injection electrode, Alq_3 as the active medium, and Al/Ca as electron-injection electrode. (b) Schematic of the pulsed EDMR experimental setup used in this study.

schematically depicted in Fig. 1(b). For measurements of current transients following the MW excitation as a function of magnetic field [8,16,30,33], as shown in Fig. 2, the output voltage of the current amplifier is recorded by the built-in fast digitizer of the E580 system. In this setup, a band-pass filter with a cutoff frequency at 30 Hz and 30 kHz is adjusted within the transimpedance amplifier. The measurement sequence is repeated at a shot-repetition rate of 454 Hz.

To observe the characteristics of coherent charge-carrier spin motion in pulsed EDMR measurements, we first conduct electrically detected charge-carrier spin-Rabi oscillation measurements, in which the duration of the pulsed MW excitation and, thus, the flip angle of the MW pulse is gradually increased, causing coherent periodic propagation between the spin eigenstates. The frequency spectrum

of these Rabi oscillations reflects the Hamiltonian and, therefore, the physical nature (spin manifold, spin interactions, coherence decay, dephasing dynamics, etc.) of the involved spin states [7,8,11]. For experiments on Alq_3 processes reported here, we record the propagation of device current changes as functions of time for 16.38 μs, starting 2 μs after the MW pulse to account for the rise time of the detector [11,30,31,33,34]. For the observation of spin-Rabi oscillation, the pulse-length dependence of the current changes is measured. For this, the device current is integrated through an analog boxcar integrator (Stanford Research Systems SR250) with an integration interval of 15 μs, starting 2 μs after the end of the pulse sequence. For these measurements, the high-pass filter of the transimpedance amplifier is used with a cutoff frequency of 10 Hz and the gain is set to 20 μA/V. The pulse sequence used for these experiments is depicted in the inset of Fig. 3(a).

For measurements of the spin-coherence times of charge-carrier pairs in Alq_3 OLEDs, we conduct electrically detected Hahn echo measurements, where we apply a modified $\pi/2 - \tau' - \pi - \tau - \pi/2 - \int Idt$ pulse sequence that is described in detail in Refs. [8,34–38]. The final $\pi/2$ read-out pulse within this sequence is required to project the spin ensemble onto their eigenstates along the direction of the external magnetic field, where the echo amplitude is detected as charge signal. The echo shape is detected by varying τ with respect to τ', with the echo maximum occurring at $\tau = \tau'$. The echo sequence is illustrated in Fig. 3(i).

Continuous-wave EDMR measurements conducted at various excitation frequencies allow for a discrimination of frequency-independent and frequency-dependent spectral line-width contributions. The frequency-independent components consist mostly of unresolved hyperfine couplings between the charge-carrier spins and the surrounding nuclear spin ensemble. These can be regarded as a randomly oriented slowly varying magnetic field, which leads to an inhomogeneous broadening of the magnetic resonance line. On the other hand, the weak, but non-negligible, spin-orbit coupling in organic materials influences the charge-carrier g factor and leads to anisotropic g tensors, distributions of g factors (g strain), and differences between the g factors of the involved spin species (i.e., the Δg effect) [8,28,29,39].

Multifrequency EDMR experiments are conducted using a series of custom-built EDMR detection probe heads, which fit inside the Oxford CF935 cryostat of the E580 spectrometer. These probe heads employ coplanar waveguide resonator structures for GHz-range excitation and radiofrequency coils for MHz-range excitation, covering together a wide range of excitation frequencies. Multifrequency EDMR experiments allow frequency-dependent and frequency-independent line broadening effects to be distinguished [8,19,28,29,35,39]. For these experiments are a separate MW source (Agilent N5181A is used for frequencies below 6 GHz while an Agilent N5173B is used for frequencies above 6 GHz), together with a MW amplifier (Mini-Circuits ZHL-5W-1) that is directly connected to the probe head. For these multifrequency EDMR experiments, changes in device currents are detected, again using the SR570 transimpedance amplifier, with a sensitivity of 2 μA/V and band-pass filters with upper and lower cutoff frequencies of 30 Hz and 30 kHz, respectively. For these multifrequency experiments, the output of the current amplifier is connected to the input of the lock-in amplifier that is part of the E580 system. We use amplitude-modulated lock-in detection [17] with source frequencies between 100 MHz and 5.55 GHz and magnetic-field-modulated lock-in detection for source frequencies between the X band and 16.885 GHz.

III. RESULTS AND DISCUSSION

Figure 2(a) displays a color plot of device current changes from the steady state at room temperature, following a 400-ns-long MW pulse at a MW power of approximately 1 kW as a function of time after the excitation pulse at $t = 0$ (horizontal axis) and the magnetic

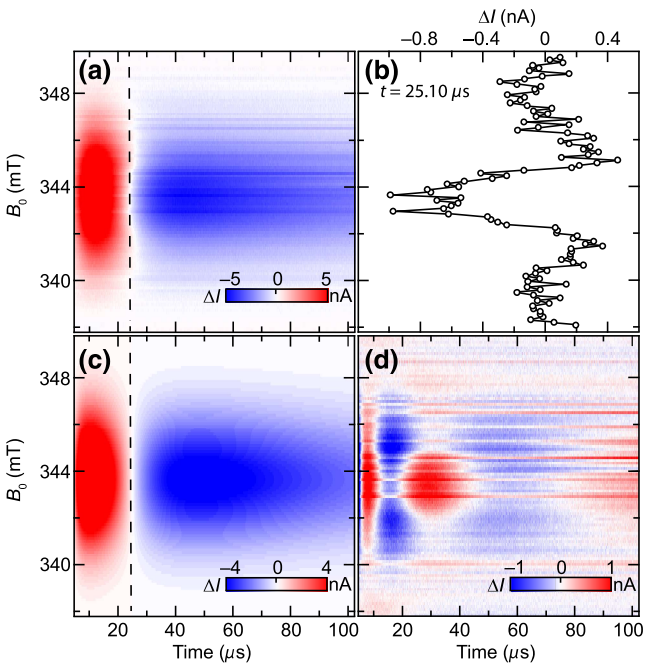

FIG. 2. (a) Plot of the OLED current change following a short MW pulse (at time $t = 0$; 400 ns duration, frequency 9.632 GHz, power 1 kW) as a function of time and applied static magnetic field B_0. (b) Plot of data from panel (a) recorded at $t = 25.10$ μs (a time where the current change reverses sign). (c) Least-squares fit result of the data in panel (a) using a two-dimensional model, taking the spectral line shape and time dependence into account as described in Ref. [5]. (d) Plot of the fit residuals, i.e. differences between measured data in (a) and fit result in (c).

field (vertical axis) in a magnetic field range that includes, for a given frequency, the magnetic resonance of vacuum electrons ($g \approx 2.0023$) at about 343.6 mT. The steady-state device current for these measurements is 50 μA. In the displayed data set, nonresonant, i.e., magnetic-field-independent current changes due to pulsed excitation, are subtracted through a zeroth-order baseline correction, i.e., a constant. The data show a pronounced magnetic resonant response at $g \sim 2$, consisting of a signal that displays a short initial current enhancement, followed by a long slow quenching, which lasts well beyond the recorded time range of 100 μs.

The general trend of the device current as a function of time and magnetic field following a pulsed MW excitation, shown in Fig. 2(a), is qualitatively similar to that seen in other OLED materials [8,16,30,33]. Harneit *et al.* [33] have modeled the observed field-dependent current transients using the product of a field-dependent term, $Y(B_0)$, and a time-dependent term, $I(t)$. The field-dependent term

$$Y(B_0) = \frac{1}{\sqrt{2\pi}\,\Delta B_{1/2,1}} e^{-\left(\frac{B_0 - B_{c,1}}{\sqrt{2}B_{1/2,1}}\right)^2} + \frac{\left(\frac{1}{r}\right)}{\sqrt{2\pi}\,\Delta B_{1/2,2}} \times e^{-\left(\frac{B_0 - B_{c,2}}{\sqrt{2}B_{1/2,2}}\right)^2}, \quad (1)$$

reflects the double-Gaussian spectral line shape, where B_0 is the magnetic field, $B_{c,1}$ and $B_{c,2}$ are the line centers, $\Delta B_{1/2,1}$ and $\Delta B_{1/2,2}$ are the full width at half maximum (FWHM) line widths of both Gaussians, and r is their weight ratio [28]. The time-dependent term

$$I(t) = \left(1 - e^{-\frac{t-t_d}{t_s}}\right) \sum_{j=1}^{2} I_j e^{-\frac{t-t_d}{\tau_j}}, \quad (2)$$

is described by parameter t_s, which is the rise time of the detector; t_d is the pulse trigger delay; as well as I_j and τ_j, which are the multiexponential weights and time constants. These parameters govern the dynamics of the spin-dependent processes that is described by this term, i.e., weakly spin-coupled electron-hole pairs that are generated under bipolar charge-carrier injection conditions, which undergo spin-dependent recombination transitions. These so-called polaron pairs are found to dominate EDMR (and ODMR) responses in organic materials, mostly conjugated polymers, with weak spin-orbit coupling and strong spin-selection rules [9].

We attempt to describe the field-dependent current transients shown in Fig. 2(a) with such a model using a nonlinear least-squares fitting procedure on the entire data set to extract the various parameters. While describing the data, to some degree, the model does not allow for a residual-free fit of the experimental data set, as shown in Fig. 2(d), which plots the difference between the best-fit result and measured data. Figure 2(b) shows a magnetic field slice of the two-dimensional residual data set, corresponding to a time $t = 25.10$ μs, as indicated by a vertical dashed line in Figs. 2(a) and 2(c). This plot reveals features that are inconsistent with a simple polaron pair process, as the model would require the field-dependent slice to vanish between signal enhancement and signal quenching at a time $t \approx 25.10$ μs due to the product of the field-dependent term with a vanishing time-dependent term. As this residual is not vanishing, we conclude that, while the observed spin-dependent currents responsible are largely consistent with a polaron-pair model, there are also smaller but significant deviations, indicating the presence of one or more additional spin-dependent processes that contribute to the recombination current in Alq_3 [13].

Using this signal, we conduct coherent transient nutation measurements [11,30,31] at room temperature [cf. Fig. 3(a)] and at 5 K [cf. Fig. 3(c)]. The duration of strong coherent excitation (1 kW nominal MW power) is varied between 0 and 500 ns in steps of 2 ns. The time-integrated current responses, i.e., the charges transmitted due to the pulsed excitations, are then recorded as functions of the excitation length. The measurement sequence is shown in the inset of Fig. 3(a). These experiments reveal an oscillatory behavior of the integrated spin-dependent currents, which, however, decay rather fast: at room temperature [cf. Fig. 3(a)], the oscillations decay to the noise level within at about three cycles, while at low temperatures (5 K) [cf. Fig. 3(c)] about five cycles are discernible. The envelope of the oscillations fades with a time constant of T_2^*, the dephasing time, which is found to be 20 ns at room temperature and 55 ns at 5 K.

Since the measured T_2^* places only a lower limit on the spin-spin relaxation time T_2, we attempt to measure electrically detected Hahn echoes [8,34–38] to narrow the range of possible values for T_2. The measurement sequence is shown in the left panel of Fig. 3(i). The measurements show that echo signals are not discernible for pulse delays down to $\tau = 74$ ns [cf. Fig. 3(i), right panel], which is the shortest achievable pulse delay due for the experimental setup used in this study. This indicates that T_2 of charge carriers is much shorter in Alq_3 compared with that of previously studied π-conjugated polymer layers [8,35,37] and that it is likely to be closer to the limit given by T_2^*.

Figures 3(a) and 3(c) display a least-squares fit of the observed Rabi oscillations to a model function

$$A \sin(\omega_1 t + \phi) e^{-\frac{t}{T_2^*}} + a + bt + ct^2 + dt^3, \quad (3)$$

which describes the Rabi oscillations, as well as the decay of the envelope in the time domain, and takes a polynomial baseline, $a + bt + ct^2 + dt^3$, into account. From this procedure, we obtain the dephasing time T_2^* and the oscillation frequency ω_1, which reflects the power of MW excitation and that ϕ is the phase. We find T_2^* to

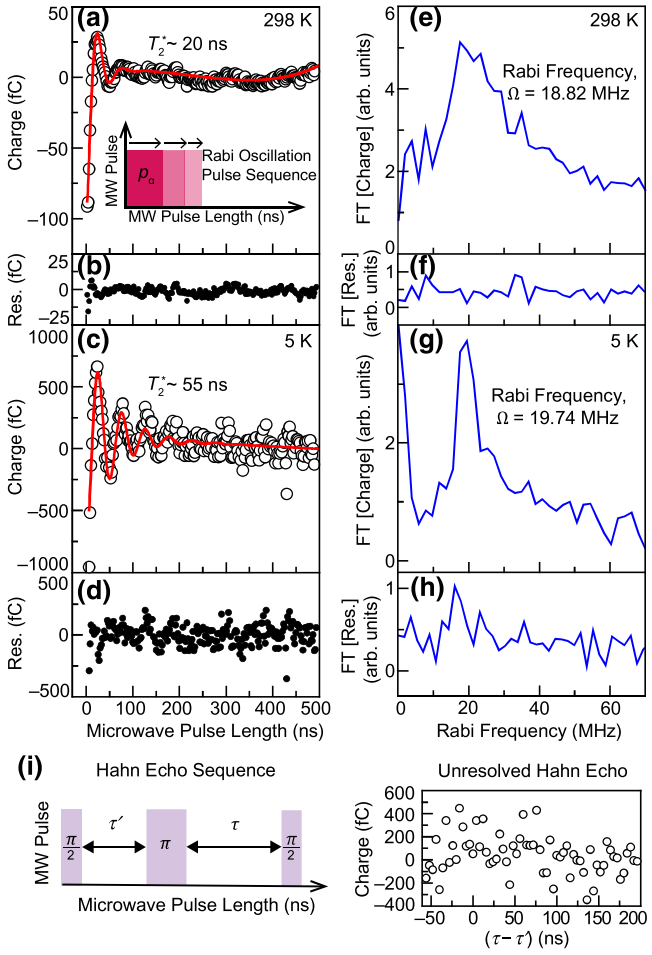

FIG. 3. (a) Integrated OLED current (open circles) as a function of pulse duration, p_α, digitally integrated over an interval of 16.38 μs, beginning 2 μs after the pulse at resonance maximum at room temperature. The pulse sequence is illustrated in the inset. The solid line represents a least-squares fit of the experimental data. (b) Residuals of the least-squares fit in panel (a). (c) Integrated OLED current as a function of pulse duration at resonance maximum at 5 K along with a least-squares fit of the experimental data. (d) Residuals of the least-squares fit in panel (c). (e) Fourier transformation of data in panel (a). (f) Fourier transformation of residuals in panel (b). (g) Fourier transformation of data in panel (c). (h) Fourier transformation of residuals in panel (d). (i) Electrically detected Hahn echo measurements at room temperature. The pulse sequence is shown on the left side, whereas, the echo signal, i.e., the integrated OLED current following the read-out pulse, is shown as a function of $\tau - \tau'$ for $\tau = 74$ ns is shown on the right side. No echo signal is discernible within the signal-to-noise ratio.

be 20 ns $\pm$ 0.8 ns at room temperature [cf. Fig. 3(a)] and 55 ns $\pm$ 15 ns at 5 K [cf. Fig. 3(c)]. If the rapid dephasing, in particular, at room temperature, is not due to spin dephasing, but rather spin relaxation, it can be attributed to the increased SOC in Alq_3 that is caused by the presence of Al. In Figs. 3(b) and 3(d), the residuals of the least-squares fit in Figs. 3(a) and 3(c) are shown. The residuals appear largely uniform, with small deviations for short pulse lengths at room temperature. In Figs. 3(e) and 3(g), we show the frequency spectrum of the data sets in Figs. 3(a) and 3(c) respectively, which are obtained via numerical Fourier transformation. In the frequency spectra, both at room temperature and at 5 K, only the fundamental frequency component at the spin-1/2 Rabi frequency is discernible, and higher frequency components are not visible. Notably, the asymmetric shoulder of this peak, which is most pronounced in Fig. 3(e), is due to the fact that the time-domain Rabi oscillations are described by modified Bessel functions [33], which give rise to an asymmetric frequency spectrum. This is most likely due to the rapid dephasing of the spin oscillations, which limits the width of the fundamental peak and obscures potential additional frequency components. In particular, a spin-beating signal at twice the fundamental Rabi frequency, due to the simultaneous excitation of both carrier spins under strong MW drive [11], is not visible at room temperature and at 5 K, which could be attributed to rapid dephasing and, therefore, the resulting limited frequency resolution of the Rabi frequency spectrum. This, however, would also imply that additional frequency components, which may be due to additional spin-dependent recombination processes in another spin manifold [7], may be present, but are obscured by the same effect, i.e., the large width of the fundamental spin-1/2 Rabi peak. We, therefore, conclude, as for the data sets shown in Fig. 2, that spin-dependent charge-carrier recombination in Alq_3 appears to be dominated by a polaron-pair process, yet the presence of additional qualitatively different spin-dependent processes cannot be excluded. To further corroborate this, we also show the frequency spectrum, which is obtained by numerical Fourier transformation, of the residuals in Figs. 3(f) and 3(h). These exhibit no significant frequency components either.

To corroborate the hypothesis expressed in the last paragraph, we consider the results of the electrically detected Hahn-echo experiment displayed in Fig. 3(i), which show unresolved echo shapes, even at the shortened available pulse delay of $\tau = 74$ ns. Data show that T_2, which describes the decay of echo amplitude with τ, must be very short, which supports the hypothesis that increased SOC causes shorter spin-spin relaxation times. Without a discernible echo signal, we cannot directly establish a value for T_2. However, because T_2^* constitutes a lower bound for T_2 ($T_2 > T_2^*$), we can estimate that 20 ns $< T_2$ at room temperature. On the other hand, from the signal-to-noise ratio of data in Fig. 3(i), we can conclude that $T_2 < 70$ ns at room temperature, because a longer spin-relaxation time would result in a detectable echo amplitude, based on the amplitude of the Rabi oscillations in Fig. 3(a), which can be used as a control experiment for the Hahn-echo null result.

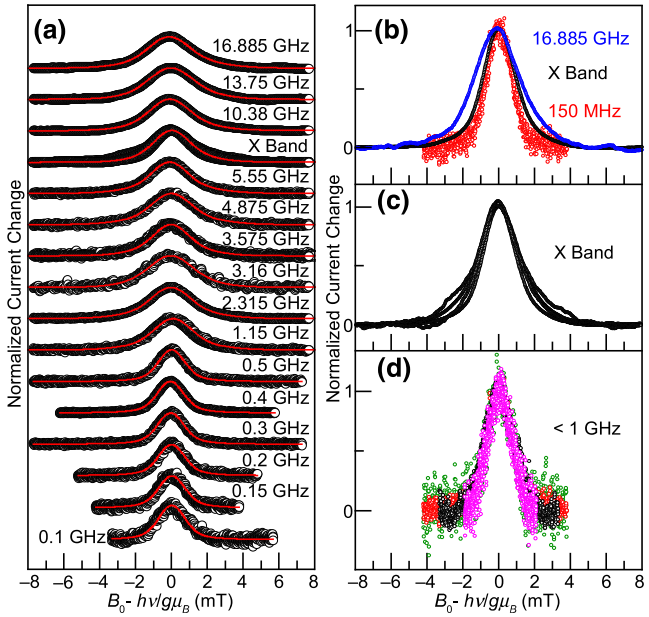

FIG. 4. (a) Multifrequency continuous-wave EDMR spectra measured at excitation frequencies ranging from 100 MHz to 17 GHz. The abscissa is normalized so that the resonance maximum occurs at zero. The spectra are normalized to show a comparable amplitude. The solid lines correspond to least-squares fits to a double-Gaussian model. (b) Comparison of spectra from panel (a) measured over the entire frequency range. (c) Comparison of spectra from panel (a) measured at X band. (d) Comparison of spectra from panel (a) measured at excitation frequencies below 1 GHz. Pronounced broadening with higher frequency and magnetic field is recognizable when X-band data are compared with data below 1 GHz. However, for the given noise levels, there are no discernable differences between line shapes obtained for different frequencies below 1 GHz.

In Fig. 4(a), the results of continuous-wave multifrequency EDMR spectra [8,28,29,35,39], measured over a frequency range from 100 MHz to about 17 GHz, are displayed. Figure 4(a) shows the zeroth-derivative spectra over the whole frequency range, as directly obtained from amplitude-modulated lock-in measurements, as well as through numerically integrated and baseline-corrected raw data sets obtained from magnetic field-modulated EDMR spectra for excitation frequencies above 5.55 GHz. The spectra are normalized to the same maximum amplitude, vertically offset, and horizontally shifted such that the resonance maxima coincide to allow for a direct comparison of line shape and width. In Figs. 4(b)–4(d), subsets of the spectra from Fig. 4(a) are shown for comparison. In Fig. 4(b), a selection of spectra covering the entire frequency range are shown superimposed to illustrate the change in line width between 150 MHz, 10 GHz, and 17 GHz. Figure 4(c) shows four spectra measured at the X band (∼10 GHz), and Fig. 4(d) shows a subset of spectra measured at frequencies below 1 GHz. We find that the FWHM line width increases with excitation frequency from 1.8 mT at the lowest frequency to 2.9 mT at the highest frequency. One remarkable feature found in Alq_3 is that, while the lower frequency spectra [below ∼1 GHz, cf. Fig. 4(d)] overlap to a large degree, the line widths at higher excitation frequencies differ widely, even for spectra recorded from nominally identical devices at the same excitation frequency under nominally identical conditions. This is illustrated in Fig. 4(c), where several cw spectra recorded at 10 GHz are plotted; the differences and variations in line width are quite pronounced. In each case, the overall EDMR line shape can be described as a superposition of two Gaussian lines with root-mean-square line widths, σ_1 and σ_2, corresponding to the two charge-carrier species [29].

The continuous-wave multifrequency analysis using the EASYSPIN toolbox [40], as shown in Fig. 4(a), exhibits the general trend that is observed in other OLED materials as well [8,28,29,35,39]: the overall line width remains constant at the lowest excitation frequencies and exhibits a substantial broadening as the excitation frequency increases. This characteristic is due to the interplay between frequency-independent and frequency-dependent inhomogeneous line-width contributions [28]. The frequency-independent width contributions arise from the unresolved hyperfine coupling between the charge-carrier spins and the nuclear spins of hydrogen, which is abundant in organic materials, and can be modeled as a slow-varying, i.e., static, distribution of local random magnetic fields, as the nuclear spin polarization is assumed to be negligible within the magnetic field range applied in this study. These resulting *hyperfine* fields lead to an inhomogeneous shift of the individual charge-carrier magnetic resonance fields and, thus, to a random line broadening. We speculate that this broadening is different for each of the two charge-carrier species due to different microscopic localization [8] of the respective molecular orbitals (highest occupied molecular orbital, HOMO, and lowest unoccupied molecular orbital, LUMO) within the Alq_3 molecule. At high magnetic field and, thus, excitation frequencies, the influence of the distributions of the charge carriers' g factors, also referred to as g strain, become increasingly relevant for the charge-carrier Larmor frequencies and, thus, for the distribution of the Larmor frequency differences within the charge-carrier pairs (the so-called Δg effect) [39]. Also, the anisotropies of the electron and hole g factors, described by g tensors, affect the resonance lines with increasing magnetic field [29]. All of these effects lead to an additional inhomogeneous line broadening that scales linearly with excitation frequency [28,34,39]. In organic materials, this broadening mechanism is found to be generally weak due to the abundance of mostly light atoms (hydrogen, carbon, oxygen) and, thus, small SOC, which causes only weak effective g factors. However, at elevated excitation

frequencies, these contributions will eventually outweigh the frequency-independent static hyperfine fields.

In Alq_3, we find a very uniform line width at excitation frequencies below 1 GHz [cf. Fig. 4(d)] for nominally identical devices measured under similar conditions. This suggests that the line-width contribution due to hyperfine fields is approximately constant and independent of the microscopic details of the sample morphology. On the other hand, the SOC-dominated lines vary considerably, even in the case of measurements under nominally identical conditions. This can be seen in Fig. 4(c), where several spectra measured at 10 GHz are plotted.

In Fig. 5, we plot the wide [cf. Fig. 5(a)] and narrow [cf. Fig. 5(b)] cw line widths measured at 200 MHz (blue data points) and at 10 GHz (red data points) as a function of OLED current, i.e., at different device operating points, adjusted by changing the device bias [cf. Fig. 1(a)], measured on the same OLED device. Values of σ_1 and σ_2, as well as the respective error bars, are determined from a nonlinear least-squares fit to a double-Gaussian model. We find that the line widths measured at 10 GHz depend only weakly on the device operating point, whereas, at 200 MHz, both line widths vary when the device current is increased.

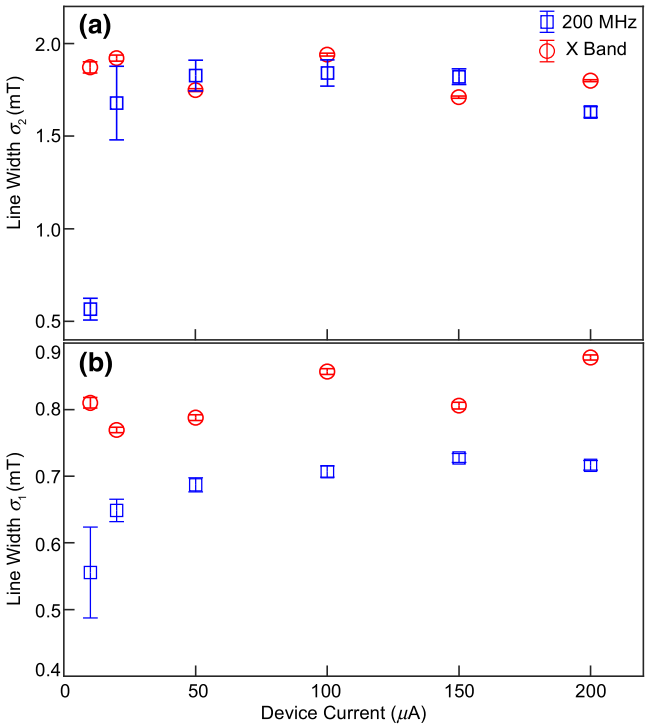

FIG. 5. Root-mean-square line widths for wide (a) and narrow (b) Gaussian resonance lines measured at 200 MHz and X band as a function of OLED current, which is established from a least-squares fit of a double-Gaussian line shape to measured spectra. The error bars correspond to parameter error estimate of the least-squares fitting procedure.

The spectra exhibit a fairly wide range of different line widths, which suggests that the effect of SOC on the g factor depends strongly on the nature of the individual devices. In addition, changes of the OLED operating point appear to influence the line width at low excitation frequencies, i.e., at 200 MHz, whereas at higher frequencies, i.e., at X band, the line widths are rather constant (cf. Fig. 5), indicating that changes of the quasi-Fermi-level enable different electronic states (e.g., different molecular orbitals) to contribute to the observed spin-dependent recombination current. A change of the device current leads to a significant modification of the unresolved hyperfine coupling. This effect is much more pronounced at lower excitation frequencies (blue data points in Fig. 5), where the overall line width is dominated by these hyperfine fields and much less pronounced at higher frequencies (red data points in Fig. 5), where SOC dominates, confirming previous observations reported in Ref. [23], where changes in the line widths of Alq_3 OLED devices as a function of current density J are reported and are interpreted to have different effects upon changing the buffer layer between the cathode-polymer interface (notably, such a buffer layer is not used in the OLED devices in this study). Given additional evidence found here that this effect is most pronounced in the low-magnetic-field domain, yet less pronounced in the high-magnetic-field domain, we can now attribute this effect do a variation of the hyperfine field strength under different bias conditions, rather than a change of SOC.

IV. CONCLUSIONS

The study of spin-dependent electronic transitions of Alq_3 under bipolar injection conditions, i.e., in Alq_3-based OLEDs under forward bias conditions, reveals the presence of more than one spin-dependent recombination process. The dynamic response of the device current following a magnetic resonant pulse under constant device bias reveals that spin-dependent recombination is dominated by intermediate electron-hole pairs, similar to previously observed polaron pair processes in OLEDs based on π-conjugated polymers. However, the significant residual of the fit using a model for this process reveals the existence of one or more additional independent spin-dependent processes, the particular nature of which is not yet corroborated. The inability to observe Hahn-echoes with pulsed EDMR, as well as the observed rapidly dephasing-spin Rabi-beat oscillations, is attributed to short coherence times of $T_2 < 70$ ns and an even shorter dephasing time, T_2^* ($\sim$20 ns), the latter both at room and at low (5 K) temperatures, indicating comparatively strong spin-orbit coupling as the cause. Multifrequency continuous-wave EDMR spectra reveal that charge-carrier line widths are governed by local hyperfine field distributions for low

frequencies (<500 MHz) and a surprisingly large variation in the SOC-dominated line widths at higher excitation frequencies, for nominally identical devices under nominally identical experimental conditions, indicating a much higher influence of morphological disorder in these experiments conducted on Alq_3, compared with previously studied conjugated polymer systems, leading to substantial fluctuations in the SOC-induced g-factor distributions. Finally, EDMR spectroscopy under varying bias conditions also reveals a variation of EDMR line width, yet only under magnetic field strengths where hyperfine fields dominate the line shape. Thus, it appears that the device's bias conditions allow tuning of the hyperfine fields that affect charge-carrier recombination.

ACKNOWLEDGMENTS

This work is supported by the National Science Foundation, NSF-DMR, Grant No. 1701427.

[1] R. Geng, H. M. Luong, T. T. Daugherty, L. Hornak, and T. D. Nguyen, A review on organic spintronic materials and devices: II. magnetoresistance in organic spin valves and spin organic light emitting diodes, J. Sci. Adv. Mater. Devices **1**, 256 (2016).

[2] D. Sun, E. Ehrenfreund, and Z. V. Vardeny, The first decade of organic spintronics research, Chem. Commun. **50**, 1781 (2014).

[3] I. Bergenti, V. Dediu, M. Prezioso, and A. Riminucci, Organic spintronics, Philos. Trans. R. Soc., A **369**, 3054 (2011).

[4] O. Ostroverkhova, Organic optoelectronic materials: Mechanisms and applications, Chem. Rev. **116**, 13279 (2016).

[5] G. Joshi, M. Y. Teferi, R. Miller, S. Jamali, M. Groesbeck, J. van Tol, R. Mclaughlin, Z. V. Vardeny, J. M. Lupton, H. Malissa, and C. Boehme, High-field Magnetoresistance of Organic Semiconductors, Phys. Rev. Appl. **10**, 024008 (2018).

[6] F. J. Wang, H. Bässler, and Z. V. Vardeny, Magnetic Field Effects in π-Conjugated Polymer-Fullerene Blends: Evidence for Multiple Components, Phys. Rev. Lett. **101**, 236805 (2008).

[7] W. J. Baker, D. R. McCamey, K. J. van Schooten, J. M. Lupton, and C. Boehme, Differentiation between polaron-pair and triplet-exciton polaron spin-dependent mechanisms in organic light-emitting diodes by coherent spin beating, Phys. Rev. B **84**, 165205 (2011).

[8] R. Miller, K. J. van Schooten, H. Malissa, G. Joshi, S. Jamali, J. M. Lupton, and C. Boehme, Morphology effects on spin-dependent transport and recombination in polyfluorene thin films, Phys. Rev. B **94**, 214202 (2016).

[9] D. R. McCamey, S.-Y. Lee, S.-Y. Paik, J. M. Lupton, and C. Boehme, Spin-dependent dynamics of polaron pairs in organic semiconductors, Phys. Rev. B **82**, 125206 (2010).

[10] T. Mori, S. Miyake, and T. Mizutani, Carrier transport and carrier trap of 8-hydroxyquinoline aluminium thin films, Jpn. J. Appl. Phys. **34**, 4120 (1995).

[11] K. J. van Schooten, D. L. Baird, M. E. Limes, J. M. Lupton, and C. Boehme, Probing long-range carrier-pair spin-spin interactions in a conjugated polymer by detuning of electrically detected spin beating, Nat. Commun. **6**, 6688 (2015).

[12] D. Sun, K. J. van Schooten, M. Kavand, H. Malissa, C. Zhang, M. Groesbeck, C. Boehme, and Z. V. Vardeny, Inverse spin Hall effect from pulsed spin current in organic semiconductors with tunable spin-orbit coupling, Nat. Mater. **15**, 863 (2016).

[13] E. Saitoh, M. Ueda, H. Miyajima, and G. Tatara, Conversion of spin current into charge current at room temperature: Inverse spin-Hall effect, Appl. Phys. Lett. **88**, 182509 (2006).

[14] F. J. Wang, Z. H. Xiong, D. Wu, J. Shi, and Z. V. Vardeny, Organic spintronics: The case of $Fe/Alq_3/Co$ spin-valve devices, Synth. Met. **155**, 172 (2005).

[15] E. Frankevich, H. Ishii, Y. Hamanaka, T. Yokoyama, A. Fuji, S. Li, K. Yoshino, A. Nakamura, and K. Seki, Formation of polaron pairs and time-resolved photogeneration of free charge carriers in π-conjugated polymers, Phys. Rev. B **62**, 2505 (2000).

[16] M. Kavand, D. Baird, K. van Schooten, H. Malissa, J. M. Lupton, and C. Boehme, Discrimination between spin-dependent charge transport and spin-dependent recombination in π-conjugated polymers by correlated current and electroluminescence-detected magnetic resonance, Phys. Rev. B **94**, 075209 (2016).

[17] S.-Y. Lee, S. Paik, D. R. McCamey, and C. Boehme, Modulation frequency dependence of continuous-wave optically/electrically detected magnetic resonance, Phys. Rev. B **86**, 115204 (2012).

[18] N. C. Greenham, J. Shinar, J. Partee, P. A. Lane, O. Amir, and F. Lu, Optically detected magnetic resonance study of efficient two-layer conjugated polymer light-emitting diodes, Phys. Rev. B **53**, 13528 (1996).

[19] W. J. Baker, K. Ambal, D. P. Waters, R. Baarda, H. Morishita, K. van Schooten, D. R. McCamey, J. M. Lupton, and C. Boehme, Robust absolute magnetometry with organic thin-film devices, Nat. Commun. **3**, 898 (2012).

[20] C. W. Tang and S. A. VanSlyke, Organic electroluminescent diodes, Appl. Phys. Lett. **51**, 913 (1987).

[21] Z. H. Xiong, D. Wu, Z. V. Vardeny, and J. Shi, Giant magnetoresistance in organic spin-valves, Nature **427**, 821 (2004).

[22] M. A. Mohd Sarjidan, N. Jubri, S. H. Basri, N. K. Za'aba, M. S. Zaini, S. N. Zaini, and W. H. Abd Majid, Fabrication and characterization of solution processed top-gate-type organic light-emitting transistor, Nanosci. Nanotechnol. Lett. **6**, 1035 (2014).

[23] G. Li, C. H. Kim, P. A. Lane, and J. Shinar, Magnetic resonance studies of tris-(8-hydroxyquinoline) aluminum-based organic light-emitting devices, Phys. Rev. B **69**, 165311 (2004).

[24] F. Comandè and J.-Ph. Ansermet, Time-resolved spin processes in Alq_3 light-emitting diode, Phys. Rev. B **90**, 201201(R) (2014).

[25] C. F. O. Graeff, G. B. Silva, F. Nüesch, and L. Zuppiroli, Transport and recombination in organic light-emitting diodes studied by electrically detected magnetic resonance, Eur. Phys. J. E **18**, 21 (2005).

[26] C. Boehme and K. Lips, Theory of time-domain measurement of spin-dependent recombination with pulsed electrically detected magnetic resonance, Phys. Rev. B **68**, 245105 (2003).

[27] P. A. Bobbert, T. D. Nguyen, F. W. A. Van Oost, B. Koopmans, and M. Wohlgenannt, Bipolaron Mechanism for Organic Magnetoresistance, Phys. Rev. Lett. **99**, 216801 (2007).

[28] G. Joshi, R. Miller, L. Ogden, M. Kavand, S. Jamali, K. Ambal, S. Venkatesh, D. Schurig, H. Malissa, J. M. Lupton, and C. Boehme, Separating hyperfine from spin-orbit interactions in organic semiconductors by multi-octave magnetic resonance using coplanar waveguide microresonators, Appl. Phys. Lett. **109**, 103303 (2016).

[29] H. Malissa, R. Miller, D. L. Baird, S. Jamali, G. Joshi, M. Bursch, S. Grimme, J. van Tol, J. M. Lupton, and C. Boehme, Revealing weak spin-orbit coupling effects on charge carriers in a π-conjugated polymer, Phys. Rev. B **97**, 161201(R) (2018).

[30] D. R. McCamey, H. A. Seipel, S.-Y. Paik, M. J. Walter, N. J. Borys, J. M. Lupton, and C. Boehme, Spin Rabi flopping in the photocurrent of a polymer light-emitting diode, Nat. Mater. **7**, 723 (2008).

[31] W. J. Baker, T. L. Keevers, C. Boehme, and D. R. McCamey, Using coherent dynamics to quantify spin coupling within triplet-exciton/polaron complexes in organic diodes, Phys. Rev. B **92**, 041201(R) (2015).

[32] C.-X. Sheng, S. Singh, A. Gambetta, T. Drori, M. Tong, S. Tretiak, and Z. V. Vardeny, Ultrafast intersystem-crossing in platinum containing π-conjugated polymers with tunable spin-orbit coupling, Sci. Rep. **3**, 2653 (2013).

[33] W. Harneit, C. Boehme, S. Schaefer, K. Huebener, K. Fostiropoulos, and K. Lips, Room Temperature Electrical Detection of Spin Coherence in C_{60}, Phys. Rev. Lett. **98**, 216601 (2007).

[34] H. Malissa, M. Kavand, D. P. Waters, K. J. van Schooten, P. L. Burn, Z. V. Vardeny, B. Saam, J. M. Lupton, and C. Boehme, Room-temperature coupling between electrical current and nuclear spins in OLEDs, Science **345**, 1487 (2014).

[35] M. Y. Teferi, J. Ogle, G. Joshi, H. Malissa, S. Jamali, D. L. Baird, J. M. Lupton, L. Whittaker Brooks, and C. Boehme, Tuning effective hyperfine fields in PEDOT:PSS thin films by doping, Phys. Rev. B **98**, 241201(R) (2018).

[36] H. Huebl, F. Hoehne, B. Grolik, A. R. Stegner, M. Stutzmann, and M. S. Brandt, Spin Echoes in the Charge Transport Through Phosphorus Donors in Silicon, Phys. Rev. Lett. **100**, 177602 (2008).

[37] W. J. Baker, T. L. Keevers, J. M. Lupton, D. R. McCamey, and C. Boehme, Slow Hopping and Spin Dephasing of Coulombically Bound Polaron Pairs in an Organic Semiconductor at Room Temperature, Phys. Rev. Lett. **108**, 267601 (2012).

[38] S.-Y. Paik, S.-Y. Lee, W. J. Baker, D. R. McCamey, and C. Boehme, T_1 and T_2 spin relaxation time limitations of phophorous donor electrons near crytstalline silicon to silicon dioxide interface defects, Phys. Rev. B **81**, 075214 (2010).

[39] G. Joshi, M. Y. Teferi, R. Miller, S. Jamali, D. Baird, J. Van Tol, H. Malissa, J. M. Lupton, and C. Boehme, Isotropic effective spin-orbit coupling in a conjugated polymer, J. Am. Chem. Soc. **140**, 6758 (2018).

[40] S. Stoll and A. Schweiger, Easyspin, a comprehensive software package for spectral simulation and analysis in EPR, J. Magn. Reson. **178**, 42 (2006).